



## Structure, mechanical properties and tribocorrosion behaviours of superhard TiSiCN nanocomposite coatings

H.Q. Wang<sup>a,b,1</sup>, H.R. Wang<sup>a,1</sup>, Y.X. Ou<sup>b,\*</sup>, X. Zhang<sup>a</sup>, Q.S. Hua<sup>a,\*</sup>, B. Liao<sup>a</sup>, X.P. Ouyang<sup>a</sup>, W.L. Zheng<sup>a</sup>, W. Fu<sup>a</sup>, X.P. Sun<sup>b</sup>, C.B. Li<sup>b</sup>

<sup>a</sup> Key Laboratory of Beam technology and Materials Modification of Ministry of Education, College of Nuclear Science and Technology, Beijing Normal University, Beijing 100875, China

<sup>b</sup> Radiation Technology Institute, Beijing Academy of Science and Technology, Beijing 100875, China

### ARTICLE INFO

#### Keywords:

TiSiCN coatings  
Superhard  
Tribocorrosion  
Visualization of cracks

### ABSTRACT

Superhard coatings are no longer very difficult to obtain, but the direct observation and prediction of their failure are still a challenge. 3D tomography of the microcracks in coating failure offers lots of new information on the geometric shape, size, and spatial structure relationship of microcracks which was not available up to now. Hence, in this work, cross-scale visualization analysis of the microcrack network in superhard yet toughness TiSiCN coatings around indentations was achieved through advanced 3D tomography combined with HRTEM characterization. TiSiCN nanocomposite coatings were deposited by high-power pulsed magnetron sputtering. Superhard TiSiCN coatings exhibit a simultaneous superhardness of  $48 \pm 6.99$  GPa and favorable toughness due to fully dense microstructure and smooth surface morphology. Due to the excellent crack initiation resistance and super-high hardness, superhard TiSiCN coatings show enhanced tribocorrosion performance in 3.5 wt% NaCl aqueous solution, with a low coefficient of friction of 0.11 and low specific wear rates of  $3.23 \times 10^{-6} \text{ mm}^{-3} \text{ N}^{-1} \text{ m}^{-1}$ .

### 1. Introduction

The service lifetimes of protective coatings for marine machinery components operating in harsh environments are highly dependent on their hardness and toughness values. High hardness means that the material has excellent resistance to plastic deformation, while high toughness represents that the material has excellent resistance to crack formation and propagation when subjected to impact loads [1]. Hard and superhard coatings with high toughness exhibit high resistance to crack formation and propagation during tribocorrosion processes [2,3]. In general, friction and corrosion failure modes of hard or superhard coatings in seawater mainly result from the friction corrosion synergistic effect [4,5]. Friction and wear lead to many fatigue microcracks that become diffusion channels for  $\text{Cl}^-$ . The diffusion of  $\text{Cl}^-$  along microcracks weakens the interfacial bonding strength, leading to coating failure [6]. Therefore, both high toughness and hardness values are important in the application of surface protective coatings for marine machinery components. However, increasing the hardness in hard

coatings often accompanies a decrease in toughness, especially for superhard nanocomposite coatings. Hence, it is still a challenge to obtain superhardness and high toughness characteristics for coatings. To date, there are many reports on obtaining superhard nanocomposite coatings by inhibiting plastic deformation, dislocation formation, dislocation activation, and grain boundary sliding by following the design criteria for nanocomposite strengthening [7]. However, there is relatively little research on the toughening mechanisms of superhard coatings. Some researchers have obtained hard nanocomposite coatings with high toughness values through coating microstructure control, such as multilayer nanocomposites and nanocrystalline/amorphous composites [8–12]; researchers have attributed their toughening mechanism to microcrack deflection and tip passivation caused by the barrier effects of nanocrystalline/amorphous composite structures on dislocation and grain boundary crack motion diffusion, limiting microcracks to a local range [13,14]. However, the mechanism of the generation and propagation of microcracks in superhard nanocomposite coatings and the mechanism of energy dissipation during the propagation of microcracks

\* Corresponding authors.

E-mail addresses: [ouyx16@tsinghua.org.cn](mailto:ouyx16@tsinghua.org.cn) (Y.X. Ou), [q.hua@bnu.edu.cn](mailto:q.hua@bnu.edu.cn) (Q.S. Hua).

<sup>1</sup> The authors contributed equally in this work.

**Table 1**  
Details parameters of the TiSiCN coatings deposition process.

Sample ( $f_{C_2H_2} = f_{N_2}$ )	$P_A$ (kW)	Pulse width ( $\mu s$ )	$V_p$ (V)	$f$ (Hz)	$I_p$ (A)	$C_2H_2$ gas flow rate (sccm)	$N_2$ gas flow rate (sccm)	Ar gas flow rate (sccm)	$V_s$ (V)	Negative bias duty cycle	substrate temperature ( $^{\circ}C$ )	process pressure (Pa)
10 sccm	6	30	720	1050	566	10	10	100	-60	90 %	125	0.72
20 sccm	6	30	692	940	659	20	20	100	-60	90 %	128	0.86
30 sccm	6	30	688	920	676	30	30	100	-60	90 %	132	0.94
40 sccm	6	30	688	900	683	40	40	100	-60	90 %	127	1.0

Note:  $P_A$ , Average target power;  $V_p$ , peak target voltage;  $I_p$ , peak target current;  $f$ , frequency of the voltage oscillation;  $V_s$ , substrate bias voltage.

have yet to be clarified. The initiation and propagation of microcracks play crucial roles in the damage and failure processes of superhard nanocomposite coatings. Some studies have revealed that the crack propagation processes in these coatings can be divided into intergranular and transgranular fractures [15,16]. However, the super-high hardness of nanocomposite coatings is often associated with high internal stresses, making it challenging to directly observe the initiation and evolution characteristics of microcracks using recent technical methods. Traditional characterization can only provide crack information on a single plane such as a surface or cross-section. 3D tomography of the microcracks during coating failure offers lots of new information on the geometric shape, size, and spatial structure relationship of microcracks which was not available up to now.

In this work, dense and low-defect TiSiCN nanocomposite coatings are deposited on AISI 304L stainless steel and Si (100) by high-power impulse magnetron sputtering (HiPIMS) in an Ar +  $N_2$  +  $C_2H_2$  mixed gas atmosphere at  $f_{N_2} = f_{C_2H_2} = 10\text{--}40$  sccm. The tribocorrosion behaviours in a 3.5 wt% NaCl aqueous solution of TiSiCN coatings deposited at different gas flow rates were studied. Based on high-resolution continuous tomography technology and high-resolution transmission electron microscopy, we have successfully conducted cross-scale visualization analysis of the structure of microcracks in superhard nanocomposite coatings with high toughness values. Our study provides new insights into the interaction between micro indentation-induced microcrack propagation and coating microstructure.

## 2. Experimental details

### 2.1. Depositions of TiSiCN coatings

TiSiCN coatings with TiSi adhesive layers were deposited on Si (100) with the dimension of 20 mm  $\times$  20 mm  $\times$  0.5 mm and AISI 304L stainless steel with the dimension of 20 mm  $\times$  20 mm  $\times$  0.5 mm by HiPIMS under mixed gases atmosphere of argon (99.99 % purity), nitrogen (99.999 % purity), and acetylene (99.95 % purity). The TiSiCN coatings deposited on the Si substrate were mainly used for composition and structural characterization, while the TiSiCN coatings deposited on AISI 304L stainless steel were mainly used for performance testing. A TiSi rectangular target (449  $\times$  75  $\times$  6 mm; Ti:Si = 4:1, 99.95 % purity) was used in the preparation of TiSi layer and TiSiCN coating by adjusting the gas atmosphere in the vacuum chamber. The TiSiCN coatings prepared under different gas flow rates were composed of TiSiCN coatings with a thickness of 2.1–3.2  $\mu m$  and TiSi buffer layers with a thickness of 0.4  $\mu m$ .

All substrates were ultrasonically cleaned with acetone, anhydrous alcohol, and deionized water for 15 min, then fixed on the sample holder in the vacuum chamber. Before starting the coating deposition procedure, the vacuum chamber gas pressure was pumped to below  $1 \times 10^{-3}$  Pa. An Ar ion source (2 kW, 150 kHz and  $\tau_{on} = 26 \mu s$ ) was used for 10 min ion sputtering cleaning program on all substrates at a bias voltage of -800 V. Then, a TiSi coating with a thickness of 0.4  $\mu m$  was deposited by sputtering TiSi target at an average target power of 6 kW and a substrate bias of -60 V (100 kHz, duty cycle 90 %) in an argon atmosphere. Finally, TiSiCN coatings were deposited on the TiSi transition layer by

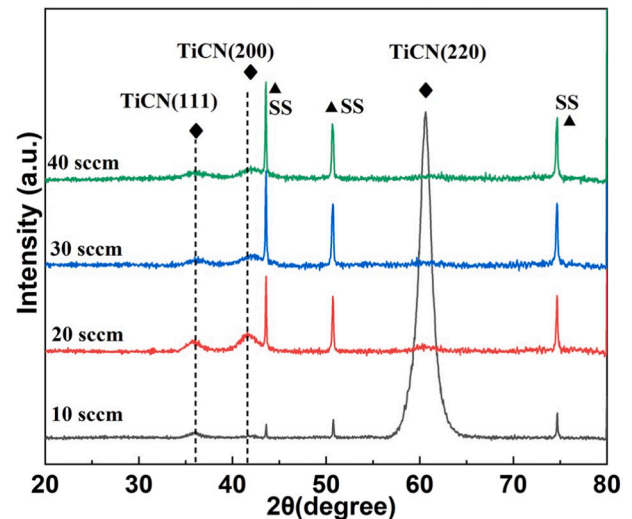


Fig. 1. XRD patterns of TiSiCN coatings deposited at  $f_{C_2H_2} = f_{N_2} = 10\text{--}40$  sccm.

sputtering the TiSi target at an average target power of 6 kW and a substrate bias of -60 V in an argon, nitrogen, and acetylene mixed gases atmosphere. The details parameters of the TiSiCN coatings deposition process were shown in Table 1.

### 2.2. Characterization

The phases and crystal structure of the TiSiCN/TiSi coatings were detected by X-ray diffraction (XRD, X'Pert PRO MPD, PANalytical); The cross-sectional and surface morphologies of TiSiCN coatings were observed by field emission scanning electron microscopy (FESEM, S-4800, HITACHI), transmission electron microscopy (TEM, Philips/FEI CM200 and Hitachi JEOL JEM-2100Plus) and atomic force microscopy (AFM, Tosca 400, Anton Paar); The composition and chemical bondings of TiSiCN coatings were identified by X-ray photoelectron spectroscopy (XPS, ESCALAB250Xi, ThermoFisher) and Raman spectroscopy (Horiba Jobin Yvon, LabRAM); A focused ion beam (FIB) system (ZEISS Cross-beam 350) was used for three-dimensional microstructure characterization; The mechanical properties of TiSiCN coatings were investigated by a nanoindenter (NanoTest system, NanoTest, Micro Materials) using a Bohrer indenter (tri-angled cone, angle between prism and centreline 65.3°, angle between prongs and centreline 77.05°, ratio of bottom edge length to depth 7.5315, radius of curvature of the end about 20 nm). Five points were selected for the nanoindenter hardness test for each sample and the final data were taken as mean values; The tribocorrosion behaviours of the coatings were evaluated by an in-situ electrochemical friction system (MFT-EC4000, HUAHUI) against  $Si_3N_4$  counterpart balls ( $\Phi 6$  mm) in 3.5 wt% NaCl aqueous solution.

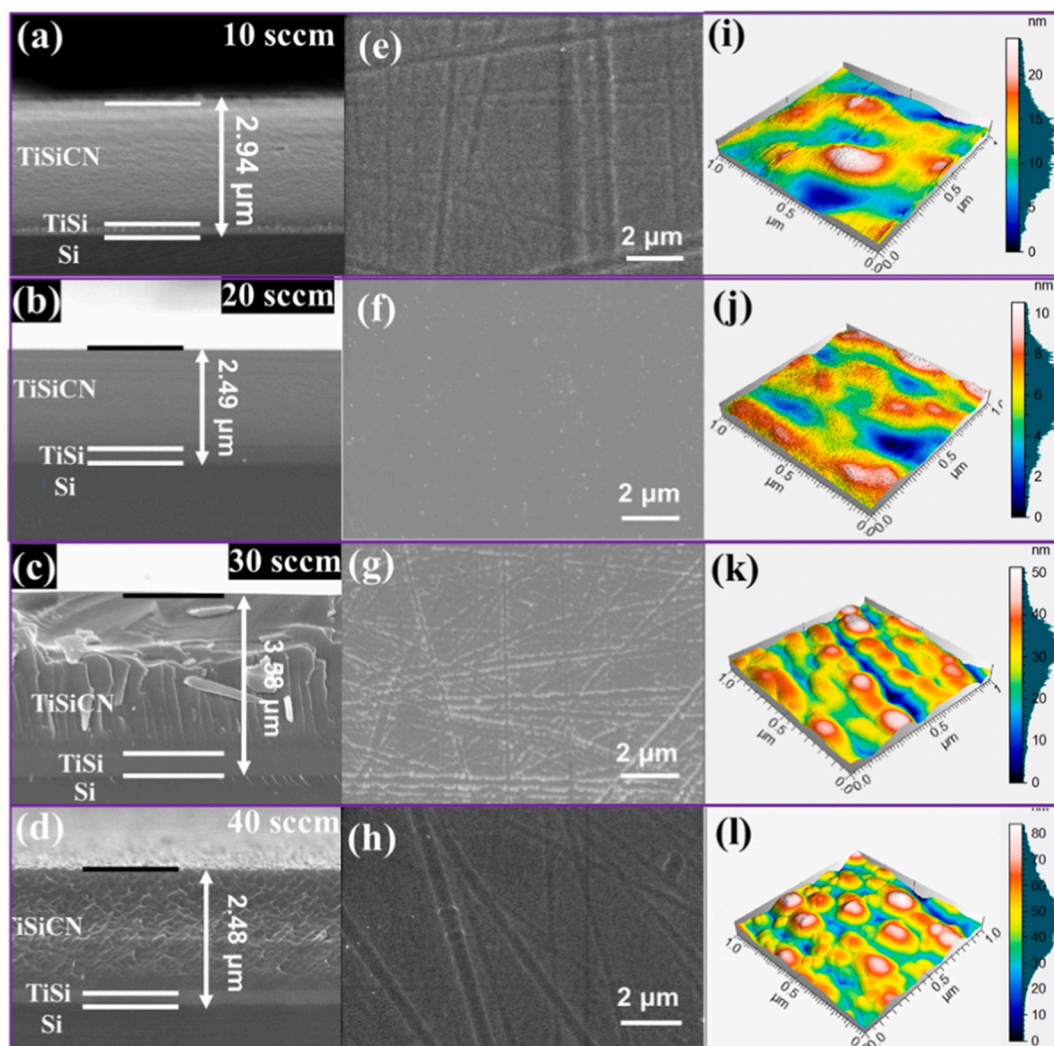


Fig. 2. Cross-sectional, surface images of SEM, and AFM surface morphologies of TiSiCN coatings deposited at  $f_{C_2H_2} = f_{N_2} = 10\text{--}40$  sccm.

### 3. Results

#### 3.1. Microstructure and composition

Fig. 1 shows the XRD patterns of TiSiCN coatings deposited on AISI 304L by HiPIMS at  $f_{C_2H_2} = f_{N_2} = 10\text{--}40$  sccm. The diffraction peaks at  $43.62^\circ$ ,  $50.70^\circ$  and  $60.29^\circ$  were labelled “SS” for AISI 304L stainless steel substrates. The diffraction peaks from TiN, TiC and TiCN were difficult to completely distinguish due to their similar face-centred structures and atomic radii. Therefore, diffraction peaks with broadening widths in TiSiCN coatings between TiN (ICDD PDF#65-4085) and TiC (ICDD PDF#32-1383) were labelled TiCN. As shown in Fig. 1, all TiSiCN coatings had face-centred cubic structures. At  $f_{C_2H_2} = f_{N_2} = 10$  sccm, TiCN nanocrystals showed strong (220) preferred orientations. With increasing  $f_{C_2H_2} = f_{N_2}$  gas flow rates, the preferred orientation of TiCN (220) in the coating disappeared and the intensity of the diffraction peaks decreases with the width increases. Previous studies had shown that the disappearance of preferred orientation is related to the formation of ultrafine nanocrystals and the transformation of nanocrystalline/amorphous composite structures [17]. In addition, no diffraction peaks from  $CN_x$ , SiC,  $Si_3N_4$  and TiSi were detected, indicating that Si was likely to exist as amorphous SiC and  $Si_3N_4$ , which has been confirmed by other published research [18,19].

Fig. 2 shows the FESEM cross-sectional, surface, and AFM surface morphologies of the TiSiCN coatings deposited at  $f_{C_2H_2} = f_{N_2} = 10\text{--}40$

sccm. The substrates of the cross-sectional image are Si, while the others images are AISI 304L. As shown in Fig. 2a–d, the thicknesses of the TiSiCN coatings increase from 2.94  $\mu\text{m}$  to 3.58  $\mu\text{m}$  as  $f_{C_2H_2} = f_{N_2}$  increases from 10 to 30 sccm. However, when  $f_{C_2H_2} = f_{N_2}$  increases to 40 sccm, the thicknesses of the coatings decrease to 2.48  $\mu\text{m}$ . TiSiCN coatings are composed of TiSi adhesive layers and TiSiCN coatings. All TiSiCN coatings present uniform and dense structures. Fig. 2e–h presents the surface morphologies of the TiSiCN coatings, revealing a highly uniform and continuous structure without visible microparticles, voids, or microcracks. The texture of the coatings originates from the stainless-steel substrate. All TiSiCN coatings exhibit highly smooth surfaces, with surface roughness values ranging from 1.43 to 12.8 nm (Sq). The highest value of Sq (12.8 nm) is observed at  $f_{C_2H_2} = f_{N_2} = 40$  sccm (Fig. 2i–l). The uniform and dense structural features of the coatings are attributed to the ion bombardment effect during deposition. During low-energy ion beam deposition, loosely bound atomic clusters are more likely to be sputtered off the surface of the coating; the heating effects of the ion beam on atoms near the surface layer of the coating promote atomic migration, resulting in a smooth and highly integrated surface structure.

Fig. 3 presents TEM investigations of the cross-sectional morphologies and selected area electron diffraction (SAED) patterns of TiSiCN coatings deposited on AISI 304L at  $f_{C_2H_2} = f_{N_2} = 10$  sccm and  $f_{C_2H_2} = f_{N_2} = 20$  sccm. As shown in Fig. 3a, there are a few irregular amorphous regions at the edges of the highly preferred nanocrystalline structures in TiSiCN coatings deposited at  $f_{C_2H_2} = f_{N_2} = 10$  sccm. The inserted SAED

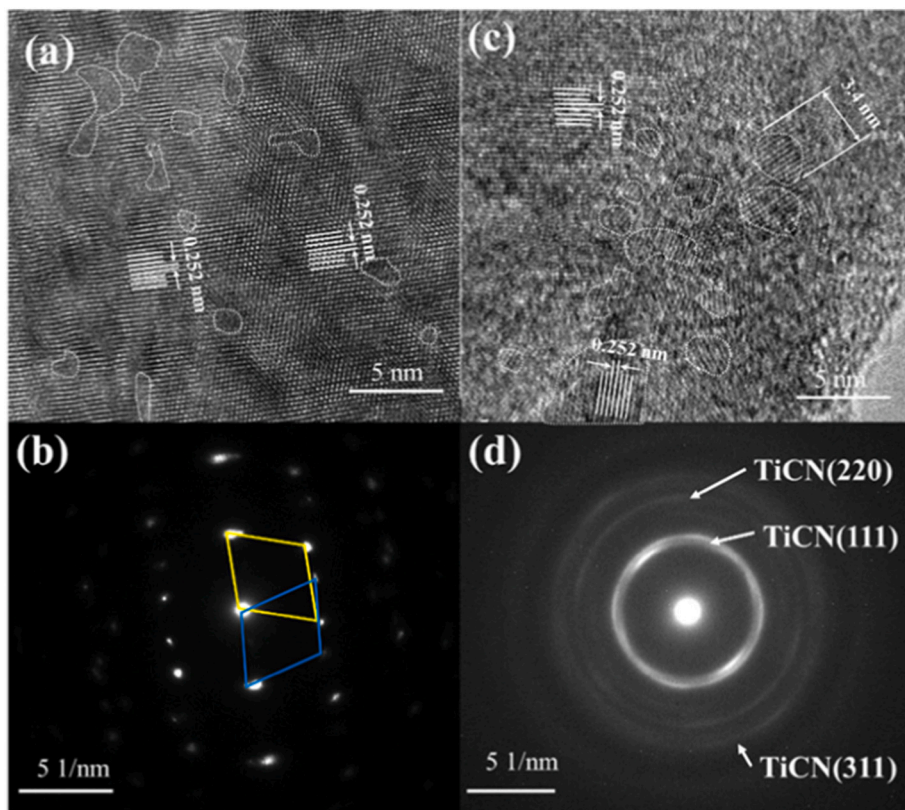


Fig. 3. TEM investigations of cross-sectional morphologies and SAED patterns of TiSiCN coatings deposited at  $f_{C_2H_2} = f_{N_2} = 10$  and 20 sccm.

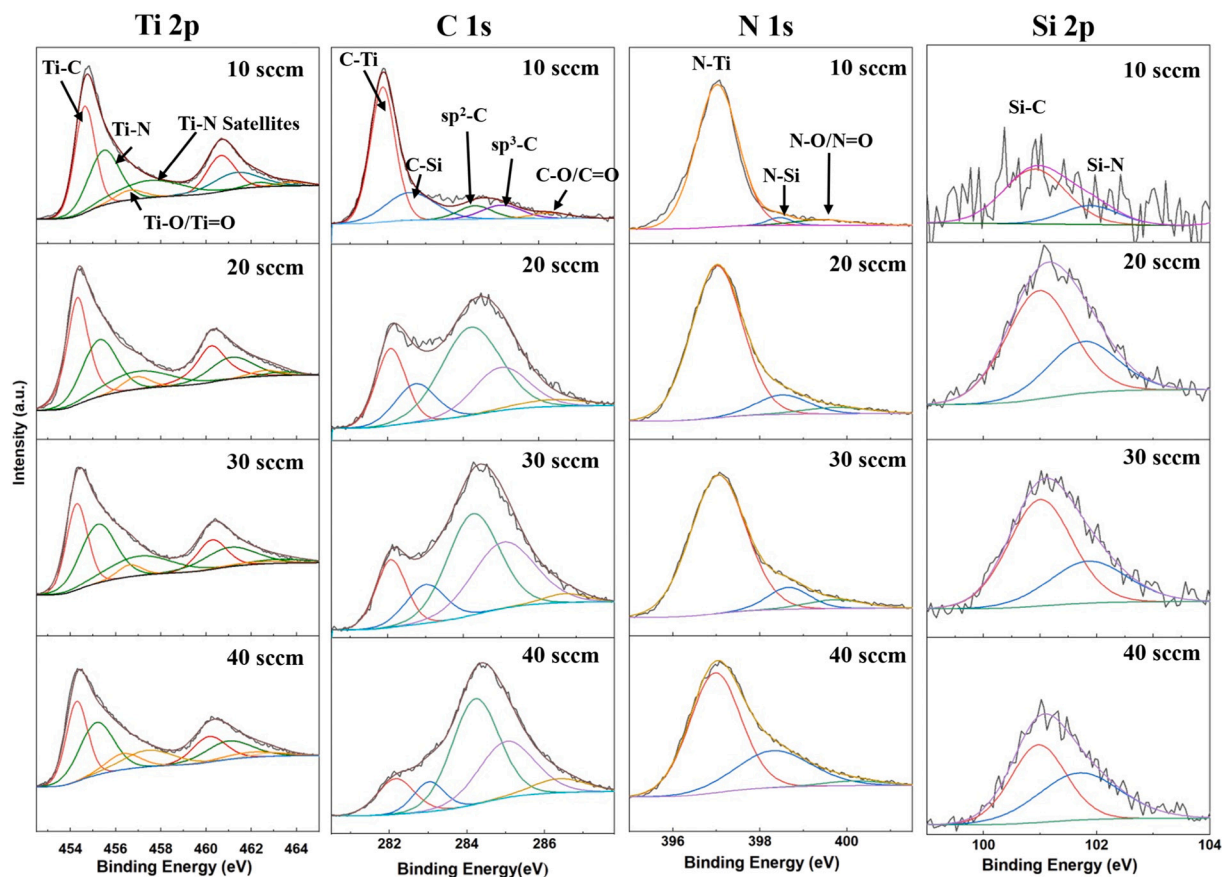
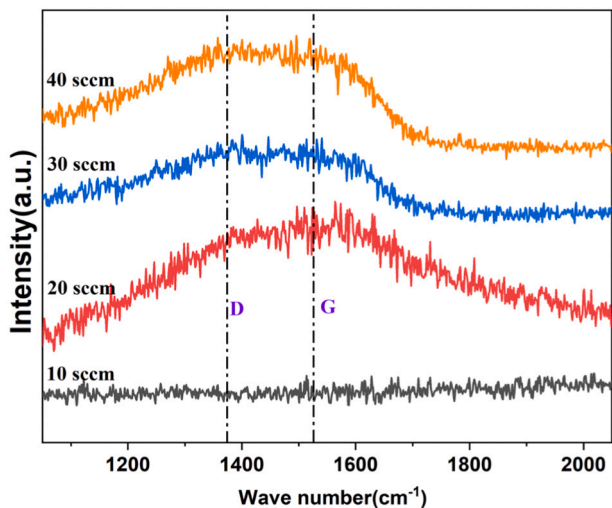


Fig. 4. XPS spectra of TiSiCN coatings deposited at  $f_{C_2H_2} = f_{N_2} = 10$ –40 sccm.

**Table 2**  
Elemental contents of TiSiCN coatings.

Sample ( $f_{C_2H_2} = f_{N_2}$ )	Ti (at.%)	Si(at.%)	C(at.%)	N (at.%)
10 sccm	45.40	4.58	23.52	26.51
20 sccm	32.35	7.42	32.39	27.84
30 sccm	29.78	4.92	40.14	25.16
40 sccm	23.74	4.09	48.53	23.64



**Fig. 5.** Raman spectra of TiSiCN coatings deposited at  $f_{C_2H_2} = f_{N_2} = 10\text{--}40$  sccm.

patterns reveal the twin structure of TiCN (Fig. 3b). As  $f_{C_2H_2} = f_{N_2}$  increases, the TiSiCN coating transforms into an amorphous coated nanocrystalline nanocomposite structure, while the TiCN

nanocrystalline structure is embedded in the amorphous structure with a grain size of approximately 3–5 nm. The inserted SAED patterns reveal distinct diffraction rings assigned to the (111), (220) and (311) reflections from the fcc crystal structure of TiCN in TiSiCN coatings (Fig. 3d). These results are in good agreement with the XRD results of Fig. 1.

Fig. 4 shows XPS spectra of TiSiCN coatings deposited on Si (100) by HiPIMS at  $f_{N_2} = f_{C_2H_2} = 10\text{--}40$  sccm. Before the start of XPS testing, a Ar ion (800 V, 60s) etching procedure was used to reduce surface contamination. The results of the coatings composition analysis after deducting the influence of oxygen showed that with the increase in  $f_{C_2H_2} = f_{N_2}$  from 10 to 40 sccm, the Ti contents in the TiSiCN coatings decreased from  $45.4 \pm 2$  at.% to  $23.7 \pm 2$  at.%; the C contents quickly increased from  $23.5 \pm 2$  at.% to  $48.5 \pm 2$  at.%, respectively; while the N and Si contents remained stable, as shown in Table 2. The trace oxygen element (less than 5 at.%) in the XPS fitting results originates from surface oxygen pollution. Core-level XPS spectra of Ti 2p, Si 2p, C 1s and N 1s in TiSiCN coatings were determined by XPS, as shown in Fig. 4. There were two main peaks in the asymmetric Ti 2p spectra, which originated from the Ti 2p<sub>3/2</sub> and Ti 2p<sub>1/2</sub> peaks at binding energies (BEs) of 455.3 and 461.3 eV. After peak differentiation and imitation, four groups of double peaks, which appeared at 455.1/461.1 eV, 456/462.1 eV, 456.9/463.5 eV, and 457.4 eV/462.4 eV, revealed the chemical bonds of Ti–C, Ti–N, Ti–N Satellites and Ti–O/Ti=O in TiSiCN coatings, respectively [20–23]. The Ti–O and Ti=O bonds were derived from Ti<sub>2</sub>O<sub>3</sub> and TiO<sub>2</sub> oxide pollutions on the TiSiCN coatings surface [24,25]. Five peaks at 281.9 eV, 283.0 eV, 284.4 eV, 285.3 eV, and 286.8 eV were obtained after imitating the C 1s peak, which corresponded to Ti–C, Si–C, sp<sup>2</sup>-C, sp<sup>3</sup>-C and C–O/C=O, respectively [25–27]. There were three peaks at 397 eV, 398.3 eV and 399.6 eV that overlapped to form a larger peak in the N 1s spectrum, which were assigned to Ti–N, Si<sub>3</sub>N<sub>4</sub> and N–C/N–O bonds [24,25]. The broad peak at 101.4 eV in the Si 2p spectrum can be fitted as two peaks (101.1 eV) and (102 eV), indicating the presence of Si–C and Si–N bonds in the

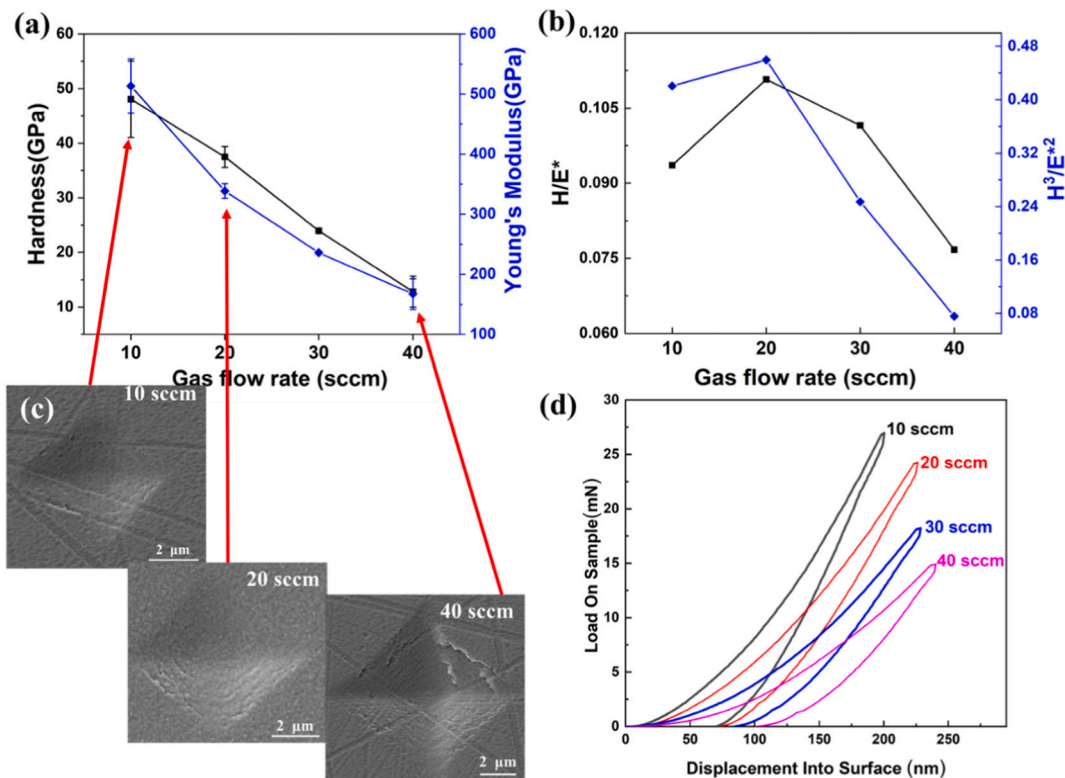


**Fig. 6.** a. The nanoindentation Hardness (H) and effective Young’s modulus ( $E^*$ ), b.  $H/E^*$  and  $H^3/E^{*2}$  ratios of TiSiCN coatings deposited at  $f_{C_2H_2} = f_{N_2} = 10\text{--}40$  sccm, c. The Micro-Vickers indentations images of  $f_{C_2H_2} = f_{N_2} = 10, 20$  and  $40$  sccm, d. the load-displacement curves of  $f_{C_2H_2} = f_{N_2} = 10\text{--}40$  sccm.

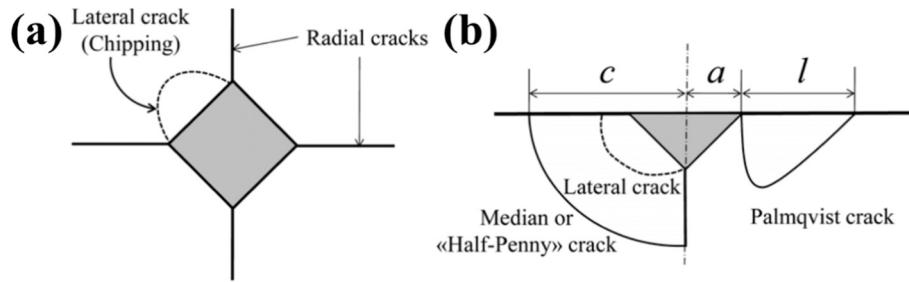


**Fig. 7.** Schematics of indentation impressions and cracks on Vickers indenters in the classical model of bulk ceramics [38]: a, surface view, b: section view. The grey area is the surface of residual impression area.

coating [24,25].

Raman spectroscopy of the TiSiCN coatings deposited on Si(100) was conducted to confirm the existence of free C, as shown in Fig. 5. The Raman peak at 1120–1750  $\text{cm}^{-1}$  comprised the D peaks (1300–1380  $\text{cm}^{-1}$ ) and G peaks (1520–1580  $\text{cm}^{-1}$ ) of amorphous carbon [28]. These bands of Raman spectra were reported in both TiC/a-C:H [29,30] and TiC/a-C:H/a-SiC:H coatings [31]. Fig. 5 shows that the TiSiCN coating prepared at  $f_{\text{C}_2\text{H}_2} = f_{\text{N}_2} = 10$  sccm had no obvious D or G peak structures, indicating that the  $\text{sp}^3\text{-C}$  and  $\text{sp}^2\text{-C}$  contents in the TiSiCN coating prepared under these conditions were very low and could be dissolved in nanocrystalline TiCN. The typical amorphous carbon peaks increased with increasing  $f_{\text{C}_2\text{H}_2} = f_{\text{N}_2}$  from 20 sccm to 40 sccm, indicating that the content of amorphous carbon in the coating increased significantly.

According to the results of HRTEM, XRD, XPS and Raman spectra, the TiSiCN coatings deposited at  $f_{\text{C}_2\text{H}_2} = f_{\text{N}_2} = 10$  sccm exhibits a nanocomposite structure composed of nanoscale amorphous clusters around TiCN nanocrystalline grain boundaries, and the amorphous phase is composed of the mixture of  $\text{Si}_3\text{N}_4$  and SiC. As  $f_{\text{C}_2\text{H}_2} = f_{\text{N}_2}$  increase, the relative content of the amorphous phase in TiSiCN coatings rapidly increases, resulting in an amorphous-coated TiCN nanocrystalline nanocomposite structure. Moreover, the composition of the amorphous phase changes from  $\text{Si}_3\text{N}_4$  and SiC to the mixture of  $\text{Si}_3\text{N}_4$ , SiC, and amorphous carbon ( $\text{sp}^2\text{-C}$  and  $\text{sp}^3\text{-C}$ ).

### 3.2. Mechanical properties

Fig. 6 exhibits the hardness (H), effective Young's modulus ( $E^*$ ),  $H/E^*$ ,  $H^3/E^{*2}$  ratios, the Micro-Vickers indentations images of TiSiCN coatings deposited on AISI 304L at  $f_{\text{C}_2\text{H}_2} = f_{\text{N}_2} = 10, 20$  and 40 sccm, and the nanoindentation load-displacement curves of  $f_{\text{C}_2\text{H}_2} = f_{\text{N}_2} = 10\text{--}40$  sccm. The hardness of the coatings is based on nanoindentation tests using a continuous stiffness measurement with a maximum displacement limit of 250 nm. The nano hardness (H) and elastic modulus (E) of the coatings were calculated using the well-known Oliver-Pharr methods [32]. Typical indentation loading-unloading curves were shown in Fig. 6d. As shown in Fig. 6a, the values of H and  $E^*$  of the TiSiCN coating deposited at  $f_{\text{C}_2\text{H}_2} = f_{\text{N}_2} = 10$  sccm are  $48 \pm 6.99$  GPa, 513.3 GPa, respectively. As  $f_{\text{C}_2\text{H}_2} = f_{\text{N}_2}$  increases to 40 sccm, H and  $E^*$  gradually decrease to 12.8 GPa and 167.1 GPa. The elasticity indices  $H/E$  and plasticity indices  $H^3/E^{*2}$  of TiSiCN coatings were plotted in Fig. 6b. Both  $H/E$  and  $H^3/E^{*2}$  increase to optimal values of 0.11 and 0.459 GPa when  $f_{\text{C}_2\text{H}_2} = f_{\text{N}_2} = 20$  sccm. However, super-high hardness ( $48 \pm 6.99$  GPa) is obtained for the TiSiCN coating deposited at  $f_{\text{C}_2\text{H}_2} = f_{\text{N}_2} = 10$  sccm, with relatively high  $H/E$  and  $H^3/E^{*2}$  values of 0.094 and 0.42 GPa, respectively.  $H/E$  represents the crack resistance under the load, and  $H^3/E^{*2}$  describes the resistance to plastic deformation; a positive correlation between fracture toughness and  $H/E$  (and  $H^3/E^{*2}$ ) has been widely reported [31,33,34]. To further characterize the toughness of the TiSiCN coatings, the Micro-Vickers indentations images of the

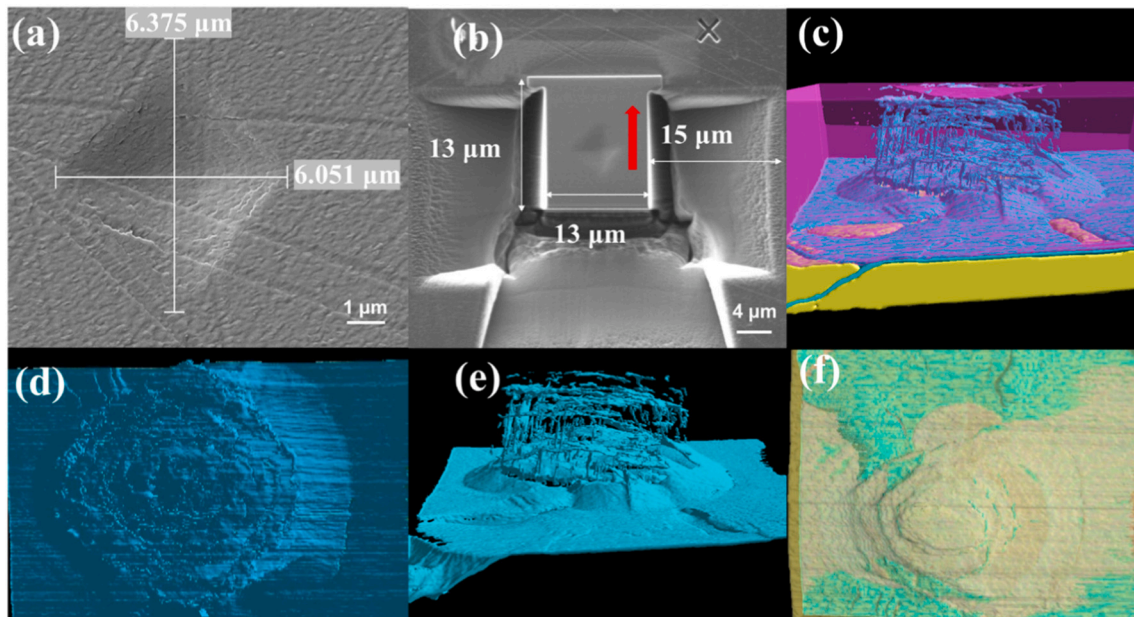


**Fig. 8.** Characterization process and three-dimensional structure diagram of indentation microcracks: a. SEM micrograph of Vickers indentation, b. FIB processing diagram, c. 3D reconstruction of the microcracks network structure in TiSiCN coating, d. the top view of the microcracks network structure, e. the side view of the microcracks network structure, f. the bottom view of the microcracks network structure.

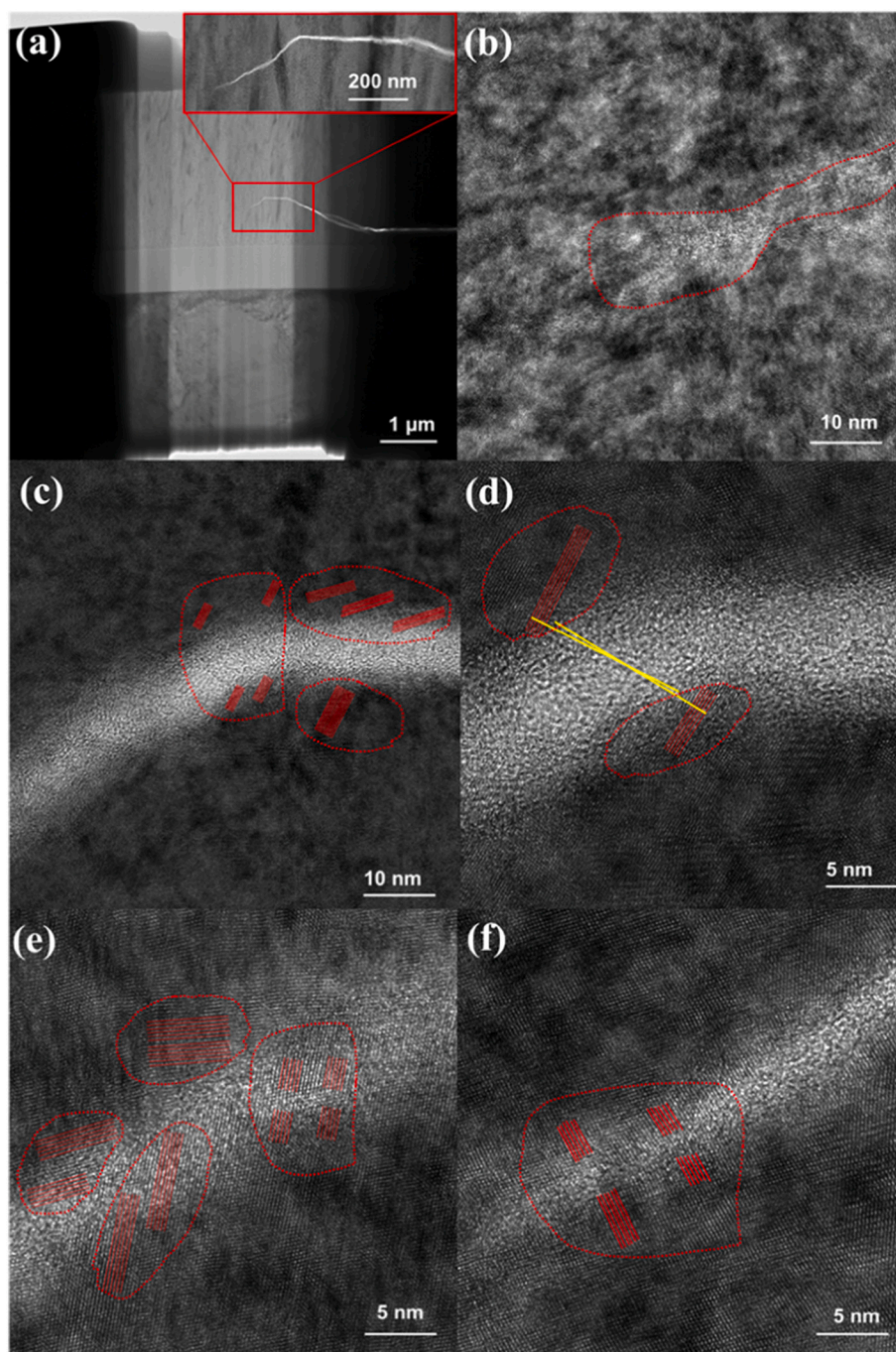


**Fig. 9.** TEM investigations of the tips of microcracks in the cross-sectional morphologies of TiSiCN coatings deposited at  $f_{C_2H_2} = f_{N_2} = 10$  sccm.

coatings at 0.25 N load with were shown in Fig. 6c. No radial cracks and slight edge microcracks of Micro-Vickers indentations are observed in coatings deposited at  $f_{C_2H_2} = f_{N_2} = 10$  and 20 sccm, indicating a high fracture toughness [7,17]. Thus, TiSiCN coatings deposited at  $f_{C_2H_2} = f_{N_2} = 10$  sccm exhibits superhard and toughness features. Moreover, the mechanism of the superhard yet tough properties of TiSiCN coatings deposited at  $f_{C_2H_2} = f_{N_2} = 10$  sccm can be attributed to the obstruction of dislocation motion and microcrack expansion by dense nanocrystalline grains and nanocrystalline/amorphous interfaces, as well as the contribution of solution strengthening of TiCN nanocrystals by heterogeneous atoms. As  $f_{C_2H_2} = f_{N_2}$  increase, the relative content of the amorphous phase in TiSiCN coatings rapidly increases. The interparticle distances between TiCN nanocrystals increase and cracks expand in the amorphous structure under mechanical loading, leading to a rapid

decrease in mechanical properties.

### 3.3. Crack resistance

Indentation-induced cracks can be used to directly reflect the fracture toughness values and deformation behaviours of coatings. The classical model describing elastic/plastic indentation damage in ceramics divides the cracks induced by elastic/plastic contact on ceramic surfaces into two primary systems: the “median/radial” system and the “lateral” system [35–37]. Fig. 7 shows the schematics of indentation impressions and cracks on Vickers indenters in the classical model of bulk ceramics [38]. The radial cracks (also known as the palmqvist cracks) are usually formed at the boundary of a plastic indentation (mainly at the top corner of the indentation) and extends outward along

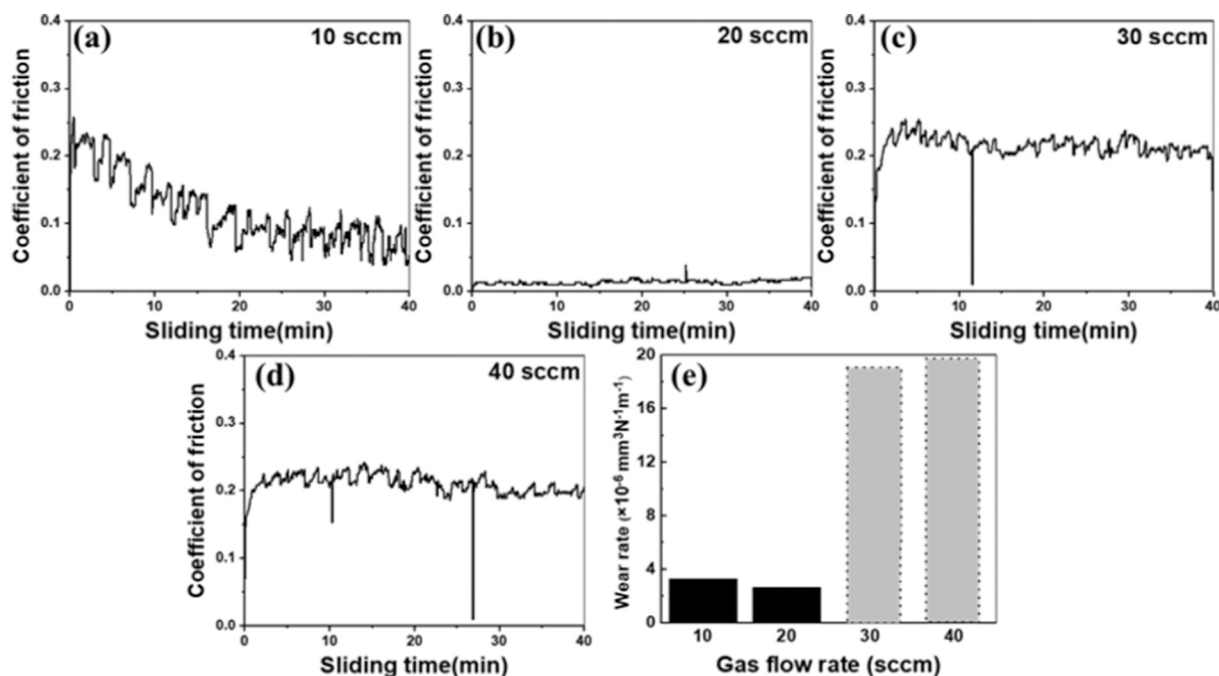


Fig. 10. Coefficient of friction and wear rates of TiSiCN coatings deposited at  $f_{C_2H_2} = f_{N_2} = 10\text{--}40$  sccm in 3.5 wt% NaCl aqueous solution.

the specimen surface in the shape of an elongated half-ellipse; the median cracks are formed at the boundary of the elastic/plastic deformation zone inside the material below the indenter and extends around in an axial direction parallel to the loading direction of the indenter in the shape of a circle or notch; the lateral cracks are formed below the deformation zone of the indentation and extends parallel to (or approximately parallel to) the surface of the specimen in the shape of a circle or disc-shaped.

To study the toughening mechanisms of superhard TiSiCN coatings deposited on AISI 304L at  $f_{C_2H_2} = f_{N_2} = 10$  sccm, a novel three-dimensional reconstruction combined with HRTEM was used to achieve cross-scale characterization of the microstructure evolution characteristics of microcracks in nanocomposite coatings. First, an indentation was pressed on the surface of the coating using a Vickers hardness tester under a load of 0.25 N (Fig. 8a). Subsequently, a notch was processed around the indentation using FIB (Fig. 8b). Then, layer-by-layer collections of the cross-sectional morphologies and etching cycles were conducted along the direction indicated by the arrow; the obtained layer-by-layer data were fitted into a 3D structure (Fig. 8c). The 3D reconstruction has a resolution of  $12 \times 12 \times 10$  nm, and the total model size is  $10.1 \times 4.4 \times 8.3$   $\mu\text{m}$ , with 830 pieces of data. The 3D reconstruction results of the coatings were presented in Fig. 8c, where pink represents the coatings, yellow represents the transition layers, and dark blue represents the crack network structures. Furthermore, Fig. 8e–f present the top view, the side view, and the bottom view of the microcracks network structure of the TiSiCN coating, respectively. The 3D structure reconstruction process was based on optimized artificial intelligence algorithms, effectively identifying the fine crack structures in the coating. The data processing can be divided into four steps, among which the “Slice Registration process” uses the “Sum of Squared Difference algorithm”; The “Artifacts Removal process” adopts the “Vertical Descending algorithm”; The “Smoothing process” adopts the “Non-Local Means algorithm”; The “Segmentation process” adopts the “Deep Learning algorithm”. This novel technique has enabled us to better understand the microstructure evolution characteristics of microcracks in TiSiCN coatings, which helps investigate the toughening mechanisms of these superhard, toughness coatings.

In the 3D tomography images of indentation-induced microcracks in

TiSiCN coatings deposited at  $f_{C_2H_2} = f_{N_2} = 10$  sccm in Fig. 8a, c–g, both cracks on the surface and cracks in the interior are visible. The scattered small number of cracks on the surface (Fig. 8a) may be related to the template morphology of the substrate, and they are not connected to the internal crack network of the coating. According to the 3D tomography images, the spatial distribution of cracks in the superhard TiSiCN coatings can be classified into “lateral” systems, which are parallel to the coating surface, and “median” systems, which are approximately parallel to the indentation loading direction (Fig. 8c–f). Radial cracks are usually observed near the indenter corner when the critical radial stress is reached in the brittle film. Meanwhile, as the toughness values of the coatings increase, radial cracks extending along the diagonals of the indentation are suppressed [39]. No radial cracks were observed in TiSiCN coatings when the Vickers hardness indentation load reached 0.25 N. This indicates a favorable fracture toughness of the superhard TiSiCN coatings deposited at  $f_{C_2H_2} = f_{N_2} = 10$  sccm.

Previous studies have shown that cracks in hard coatings deposited on plastic substrate surfaces are mainly caused by bending tensile stresses [40,41]. The deformation of the substrate under compressive force causes a loss of mechanical support for the coating, resulting in the generation of bending tensile stresses. Simulation studies on stress evolution during the indentation process have revealed that the highest tensile stress occurs at the centre and edge of the indentation surface [40,42]. As a result, median cracks are formed below the indenter projection parallel to the ballast direction.

The formation of lateral cracks parallel to the surface can be explained by the elastic recovery of the coating/substrate system during indentation unloading process [43]: During the unloading period of the micro indenter, the elastic recovery of the coating is much higher than that of the plastic deformation substrate, resulting in tensile stress parallel to the surface (As shown in Fig. 8f). The superhard coating with highly effective Young’s modulus (513.3 GPa) accumulates high elastic strain energy during loading, resulting in the tensile stress parallel to the surface to exceed the resistance against lateral cracking (inside the coating and at the interface with the substrate). Thus, lateral cracks form at the coating/substrate interface and within the coating.

To further study the propagation mechanisms of microcracks in TiSiCN nanocomposite coatings, based on 3D reconstruction structural

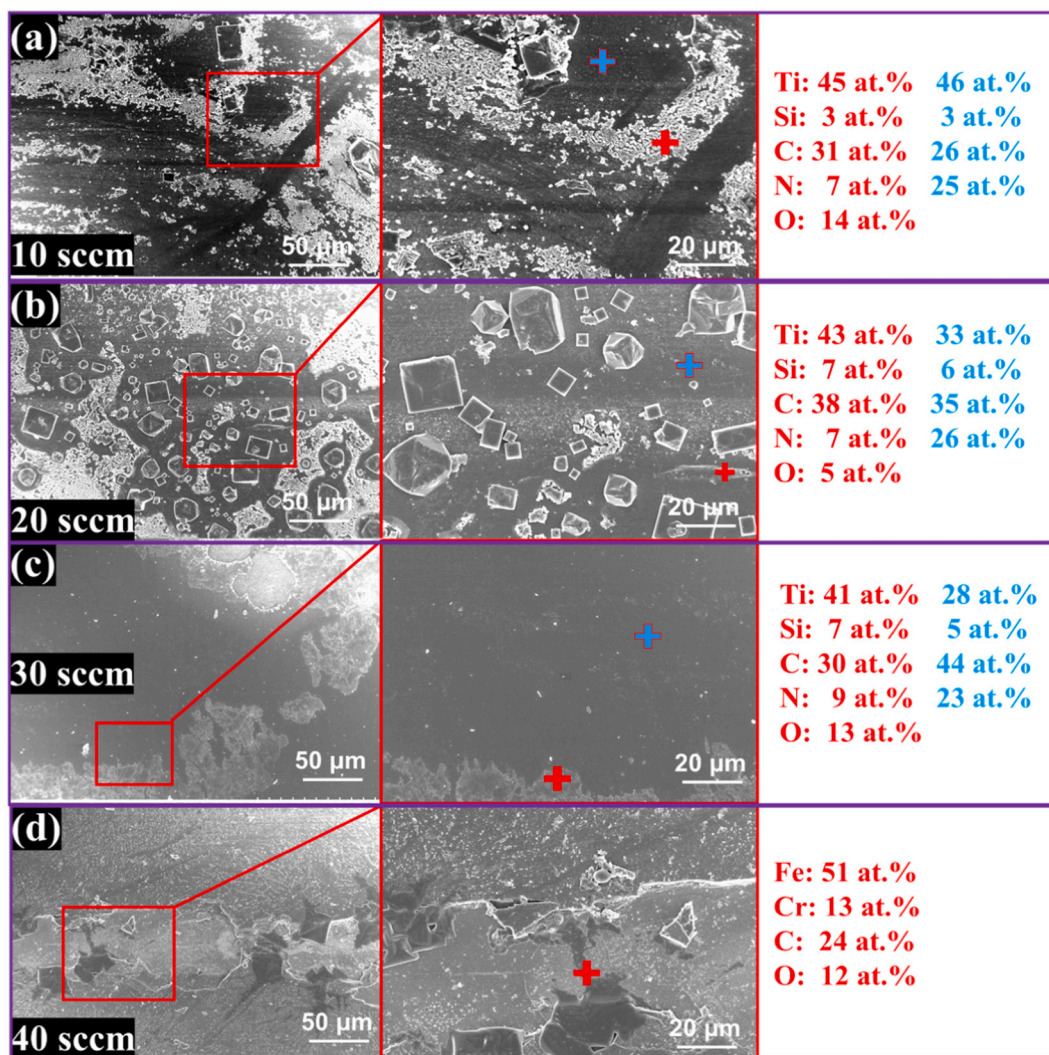


**Fig. 11.** Surface morphology and EDS results of the wear scars and debris of TiSiCN coatings deposited at  $f_{C_2H_2} = f_{N_2} = 10\text{--}40$  sccm in 3.5 wt% NaCl aqueous solution.

analysis, a TEM sample is prepared by using FIB to peel a single microcrack region at the edge of the indentation under the same load. Fig. 9 showed the TEM investigations of the tips of microcracks in the cross-sectional morphologies of TiSiCN coatings deposited at  $f_{C_2H_2} = f_{N_2} = 10$  sccm. As shown in Fig. 9, the microcrack propagation in the superhard TiSiCN coating is initially relatively straight (approximately 350 nm), with multiple deflections during propagation (Fig. 9a) and significant passivation of the crack tip (Fig. 9b). When a crack encounters a nanocrystalline interface in the TiSiCN coating, it undergoes deflection, leading to a long and tortuous propagation path. This process consumes additional energy, enhancing the toughness of the TiSiCN coating by preventing further crack propagation. HRTEM images of the regions where cracks are greatly deflected by grain boundaries when propagating along them reveal changes in the fracture mechanism from intergranular to transgranular. Moreover, grain orientations on both sides of the crack exhibit small angle deflection, as shown in Fig. 9c and Fig. 9d. Transgranular fracture consumes more crack energy than intergranular fracture, thereby enhancing the fracture toughness values of TiSiCN coatings. When the difference between the direction of crack propagation and the angle of the grain boundary is small, the microcrack propagation direction is deflected to propagate along the nanocrystalline grain boundary, which is influenced by the characteristics of the nanocrystalline interface (Fig. 9e). Moreover, during transgranular fracture, the direction of microcrack propagation is mostly unchanged

(Fig. 9f).

The key to coatings toughening lies in the creation of complex coherent boundaries at interfaces, by which more energy is consumed during crack initiation and propagation [10]. Our results show that the deflection process of microcracks in superhard yet tough TiSiCN coatings is accompanied by the transition between intergranular fracture and transgranular fracture, which is related to the crack propagation direction and grain boundary angle. The composite fracture mode combining transgranular fracture and intergranular fracture can further improve the energy dissipation of microcracks and enhance the toughness of the coating.

### 3.4. Tribocorrosion resistance

The tribocorrosion resistance of TiSiCN coatings was evaluated by coefficients of friction (COF) and worn surface morphologies. During the reciprocating friction process, the friction length was 5 mm, the load was 1 N, and the friction frequency was 1 Hz. Fig. 10 presents the coefficient of friction and wear rates of TiSiCN coatings deposited on AISI 304L in 3.5 wt% NaCl aqueous solution. The COF of  $f_{C_2H_2} = f_{N_2} = 10$  sccm shows a trend of fluctuating downwards in tribocorrosion, and the average value is 0.11 in the friction stage. The calculated specific wear rate is  $3.23 \times 10^{-6} \text{ mm}^{-3} \text{ N}^{-1} \text{ m}^{-1}$ , which is much lower than that for the AISI 304L stainless steel substrate in our previous research ( $7.28 \times 10^{-4}$

$\text{mm}^{-3}\text{N}^{-1}\text{m}^{-1}$ ) [44]. As  $f_{\text{C}_2\text{H}_2} = f_{\text{N}_2}$  increases, the average COFs of the TiSiCN coatings present a great difference during tribocorrosion. Due to the lubrication of increased amorphous carbon, TiSiCN coatings deposited at  $f_{\text{C}_2\text{H}_2} = f_{\text{N}_2} = 20$  sccm exhibit an ultralow COF of 0.04 and a low calculated specific wear rate of  $2.57 \times 10^{-6} \text{mm}^{-3}\text{N}^{-1}\text{m}^{-1}$ . Meanwhile, TiSiCN coatings deposited at  $f_{\text{C}_2\text{H}_2} = f_{\text{N}_2} = 30$  sccm and 40 sccm show high and unstable COFs of 0.23 and 0.24, respectively. Surface morphologies and EDS results after deducting Na and Cl elements of wear scar are demonstrated in Fig. 11. The cubic crystal in the figures originates from NaCl microparticles. The regional peeling and large-scale failure of TiSiCN coating during the tribocorrosion process result in significant COF differences (Fig. 10c and Fig. 10d). TiSiCN coatings with low toughness ( $f_{\text{C}_2\text{H}_2} = f_{\text{N}_2} = 30$  sccm and 40 sccm) fail with the development of microcracks under cyclic loading stress, resulting in severe fluctuations in the COF and a rapid decline in wear resistance [45–47]. While no macrocracks are observed on the worn surfaces during sliding wear in the coatings deposited at  $f_{\text{C}_2\text{H}_2} = f_{\text{N}_2} = 10$  and 20 sccm. This indicates that TiSiCN coatings with high toughness values ( $f_{\text{C}_2\text{H}_2} = f_{\text{N}_2} = 10$  sccm and 20 sccm) can suppress the initiation and development of microcracks under cyclic stress, thereby reducing the synergistic effect of friction corrosion mainly caused by  $\text{Cl}^-$  corrosion. The results demonstrate that a superhard yet toughness TiSiCN coating ( $f_{\text{C}_2\text{H}_2} = f_{\text{N}_2} = 10$  sccm) exhibits excellent tribocorrosion resistance in a 3.5 wt% NaCl solution.

#### 4. Conclusion

In conclusion, we deposited TiSiCN coatings by HiPIMS. TiSiCN coatings deposited at  $f_{\text{C}_2\text{H}_2} = f_{\text{N}_2} = 10$  sccm exhibits an super-high hardness of  $48 \pm 6.99$  GPa and favorable toughness. The 3D tomography results of indentation-induced microcracks indicate that the spatial structure of internal microcracks in superhard yet tough TiSiCN coatings deposited on AISI 304L stainless steel substrates consists of lateral crack parallel to the surface and discontinuous median cracks structures. Based on the formation mechanism of transverse crack networks, reducing the elastic modulus of hard and tough coatings deposited on plastic substrates is expected to provide higher crack resistance performance. And the superhard TiSiCN coatings with highly tough features exhibited excellent tribocorrosion resistance performance in 3.5 wt% NaCl aqueous solution.

#### Declaration of competing interest

The authors declared no potential conflicts of interest with respect to the research, authorship, and publication of this article.

#### Data availability

Data will be made available on request.

#### Acknowledgements

This work was supported by National Natural Science Foundation of China (Grant No. 12275028), National Natural Science Foundation of China (Grant No.12175019), Key Technologies R&D Program of Guangdong Province (Grant No. 2019B090909002), 2023 innovation engineering projects (Grant No. 23CA006) and 2023 innovation cultivation project (Grant No. 23CB089) from Beijing Academy of Science and Technology, National Natural Science Foundation of China (12075031) and Natural Science Foundation of Beijing Municipality (1222022), National Natural Science Foundation of China (Grant Nos. 12105020).

#### References

- [1] S. Zhang, D. Sun, Y. Fu, H. Du, Recent advances of superhard nanocomposite coatings: a review, *Surf. Coat. Technol.* 167 (2–3) (2003) 113–119.
- [2] H. Tao, M.T. Tsai, H.W. Chen, J.C. Huang, J.G. Duh, Improving high-temperature tribological characteristics on nanocomposite CrAlSiN coating by Mo doping, *Surf. Coat. Technol.* 349 (2018) 752–756.
- [3] Y.X. Ou, H.Q. Wang, X. Ouyang, Y.Y. Zhao, Q. Zhou, C.W. Luo, Q.S. Hua, X. P. Ouyang, S. Zhang, Recent advances and strategies for high-performance coatings, *Prog. Mater. Sci.* 136 (2023), 101125.
- [4] G. Cui, Q. Bi, S. Zhu, J. Yang, W. Liu, Tribological properties of bronze graphite composites under sea water condition, *Tribol. Int.* 53 (2012) 76–86.
- [5] R.J.K. Wood, Tribo-corrosion of coatings: a review, *J. Phys. D* 40 (18) (2007) 5502.
- [6] Y. Fu, F. Zhou, Q. Wang, M. Zhang, Z. Zhou, Electrochemical and tribocorrosion performances of CrMoSiCN coating on Ti-6Al-4V titanium alloy in artificial seawater, *Corros. Sci.* 165 (2020), 108385.
- [7] S. Zhang, H.L. Wang, S.E. Ong, D. Sun, X.L. Bui, Hard yet tough nanocomposite coatings—present status and future trends, *Plasma Process. Polym.* 4 (2007) 219.
- [8] Y.M. Wang, J. Li, A.V. Hamza, T.W. Barbee, Ductile crystalline–amorphous nanolaminates, *PNAS* 104 (27) (2007) 11155–11160.
- [9] S. Zhang, D. Sun, Y. Fu, H. Du, Toughening of hard nanostructural thin films: a critical review, *Surf. Coat. Technol.* 198 (1–3) (2005) 2–8.
- [10] Y.X. Wang, S. Zhang, Toward hard yet tough ceramic coatings, *Surf. Coat. Technol.* 258 (2014) 1–16.
- [11] A.N. Ranade, L.R. Krishna, Z. Li, J. Wang, C.S. Korach, Y.W. Chung, Relationship between hardness and fracture toughness in Ti–TiB<sub>2</sub> nanocomposite coatings, *Surf. Coat. Technol.* 213 (2012) 26–32.
- [12] C. Wang, K.C. Shi, C. Gross, J.M. Pureza, M.M. Lacerda, Y.W. Chung, Toughness enhancement of nanostructured hard coatings: design strategies and toughness measurement techniques, *Surf. Coat. Technol.* 257 (2014) 206–212.
- [13] A. Riedl, R. Daniel, M. Stefanelli, T. Schöberl, O. Kolednik, C. Mitterer, J. Keckes, A novel approach for determining fracture toughness of hard coatings on the micrometer scale, *Scr. Mater.* 67:7–8 (2012) 708–711.
- [14] X. Chen, Y. Du, Y.W. Chung, Commentary on using H/E and H<sub>3</sub>/E<sub>2</sub> as proxies for fracture toughness of hard coatings, *Thin Solid Films* 688 (2019), 137265.
- [15] Q.L. Li, P. Song, X. He, X. Yu, C. Li, T.H. Huang, K.Y. Lü, Y. Zhou, J.S. Lu, Plastic metallic-barrier layer for crack propagation within plasma-sprayed Cu/ceramic coatings, *Surf. Coat. Technol.* 360 (2016) 259–268.
- [16] O. Kesler, J. Matejíček, S. Sampath, S. Suresh, T. Gnaeupel-Herold, P.C. Brand, H. J. Prask, Measurement of residual stress in plasma-sprayed metallic, ceramic and composite coatings, *Mat. Sci. Eng. A* 257-2 (1998) 215–224.
- [17] Y.X. Ou, H.Q. Wang, Q.S. Hua, B. Liao, X.P. Ouyang, Tribocorrosion behaviors of superhard yet tough Ti-C-N ceramic coatings, *Surf. Coat. Technol.* 439 (2022), 128448.
- [18] Q. Li, F.Q. Jiang, Y.X. Leng, R.H. Wei, N. Huang, Microstructure and tribological properties of Ti(Cr)SiCN coating deposited by plasma enhanced magnetron sputtering, *Vacuum* 89 (2013) 168–173.
- [19] R. Akhter, Z.F. Zhou, Z.H. Xie, P. Munroe, TiN versus TiSiN coatings in indentation, scratch and wear setting, *Appl. Surf. Sci.* 563 (2021), 150356.
- [20] J. Lauridsen, P. Eklund, J. Jensen, H. Ljungcrantz, Å. Öberg, E. Lewin, U. Jansson, A. Flink, H. Högberg, L. Hultman, Microstructure evolution of Ti–Si–C–Ag nanocomposite coatings deposited by DC magnetron sputtering, *Acta Mater.* 58-20 (2010) 6592–6599.
- [21] J.L. Lin, J.J. Moore, B. Mishra, M. Pinkas, W.D. Sproul, The structure and mechanical and tribological properties of TiBCN nanocomposite coatings, *Acta Mater.* 58-5 (2010) 1554–1564.
- [22] Y. Yao, J.L. Li, Y.X. Wang, Y.W. Ye, L.H. Zhu, Influence of the negative bias in ion plating on the microstructural and tribological performances of Ti–Si–N coatings in seawater, *Surf. Coat. Technol.* 280 (2015) 154–162.
- [23] A.M. Kia, J. Speulmanns, S. Bönhardt, J. Emara, K. Kühnel, N. Haufe, W. Weinreich, Spectroscopic analysis of ultra-thin TiN as a diffusion barrier for lithium-ion batteries by ToF-SIMS, XPS, and EELS, *Appl. Surf. Sci.* 564 (2021), 150457.
- [24] A. Hatem, J.L. Lin, R.H. Wei, R.D. Torres, C. Laurindo, G.B. Souza, P. Soares, Tribocorrosion behavior of low friction TiSiCN nanocomposite coatings deposited on titanium alloy for biomedical applications, *Surf. Coat. Technol.* 347 (2018) 1–12.
- [25] E. Thangavel, S. Lee, K.S. Nam, J.K. Kim, D.G. Kim, *Appl. Surf. Sci.* 265 (2013) 60–65.
- [26] M. Stüber, H. Leiste, S. Ulrich, H. Holleck, D. Schild, Microstructure and properties of low friction TiC-C nanocomposite coatings deposited by magnetron sputtering, *Surf. Coat. Technol.* 150 (2–3) (2002) 218–226.
- [27] Y.J. Jo, T.F. Zhang, M.J. Son, K.H. Kim, Synthesis and electrochemical properties of Ti-doped DLC films by a hybrid PVD/PECVD process, *Appl. Surf. Sci.* 433 (2018) 1184–1191.
- [28] F.C. Thompson, F.M. Kustas, G.A. Crawford, Influence of hexamethyldisilazane vapor on the structure and mechanical properties of TiC-based coatings, *Surf. Coat. Technol.* 374 (2019) 264–275.
- [29] W.J. Meng, B.A. Gillispie, Mechanical properties of Ti-containing and W-containing diamond-like carbon coatings, *J. Appl. Phys.* 84 (1998) 4314.
- [30] H.Q. Wang, Q. Zhou, Y.X. Ou, B. Liao, X. Zhang, Q.S. Hua, X.P. Ouyang, C.W. Luo, Tribocorrosion behaviors of nc-TiC/a-C:H nanocomposite coatings: In-situ electrochemical response, *Thin Solid Films* 730 (2021), 138719.
- [31] H.W. Strauss, R.R. Chromik, S. Hassani, J.E. Klemberg-Sapieha, In situ tribology of nanocomposite Ti–Si–C–H coatings prepared by PE-CVD, *Wear* 272 (1) (2011) 133–148.

- [32] W.C. Oliver, G.M. Pharr, An improved technique for determining hardness and elastic modulus using load and displacement sensing indentation experiments, *J. Mater. Res.* 7 (6) (1992) 1564–1583.
- [33] A. Leyland, A. Matthews, On the significance of the H/E ratio in wear control: a nanocomposite coating approach to optimised tribological behaviour, *Wear*. 246 (1–2) (2000) 1–11.
- [34] Y.X. Ou, H. Chen, Z.Y. Li, J. Lin, W. Pan, M.K. Lei, Microstructure and tribological behavior of TiAlSiN coatings deposited by deep oscillation magnetron sputtering, *J. Am. Ceram. Soc.* 101 (2018) 5166.
- [35] B.R. Lawn, A.G. Evans, A model for crack initiation in elastic/plastic indentation fields, *J. Mater. Sci.* 12 (1977) 2195–2199.
- [36] B.R. Lawn, A.G. Evans, D.B. Marshall, Elastic/plastic indentation damage in ceramics: I, the median/radial crack system, *J. Am. Ceram. Soc.* 63 (1980) 574–581.
- [37] D.B. Marshall, B.R. Lawn, A.G. Evans, Elastic/plastic indentation damage in ceramics: II, the lateral crack system, *J. Am. Ceram. Soc.* 65 (1982) 561–566.
- [38] A. Iost, Détermination de la ténacité de matériaux fragiles ou ductiles à partir de l'essai d'indentation, *Metall. Res. Technol.* 110 (3) (2013) 215–233.
- [39] Q. Wang, Y. Lin, F. Zhou, J. Kong, The influence of Ni concentration on the structure, mechanical and tribological properties of Ni–CrSiN coatings in seawater, *J. Alloys Compd.* 819 (2020), 152998.
- [40] M. Zawischa, Stefan Makowski, Martin Kuczyk, Volker Weihnacht, Comparison of fracture properties of different amorphous carbon coatings using the scratch test and indentation failure method, *Surf. Coat. Technol.* 435 (2022), 128247.
- [41] K.K. Fu, Y.B. Yin, L. Chang, D.H. Shou, B.L. Zheng, L. Ye, Analysis on multiple ring-like cracks in thin amorphous carbon film on soft substrate under nanoindentation, *J. Phys. D* 46 (50) (2013), 505314.
- [42] Z.H. Xie, R. Singh, A. Bendavid, P.J. Martin, P.R. Munroe, M. Hoffman, Contact damage evolution in a diamond-like carbon (DLC) coating on a stainless steel substrate, *Thin Solid Films* 515 (2007) 3196–3201.
- [43] J. Chen, S.J. Bull, Indentation fracture and toughness assessment for thin optical coatings on glass, *J. Phys. D. Appl. Phys.* 40 (2007) 5401–5417.
- [44] H.Q. Wang, Y.X. Ou, B. Liao, X.D. Ou, J. Luo, P. Pang, L. Chen, X. Zhang, Q.S. Hua, M.Y. Bao, Tribocorrosion behaviors of TiSiCN nanocomposite coatings deposited by high power impulse magnetron sputtering, *Mater. Res. Express.* 7 (2020), 076407.
- [45] Y. Wang, J.L. Li, C.Q. Dang, Y.X. Wang, Y.J. Zhu, Influence of carbon contents on the structure and tribocorrosion properties of TiSiCN coatings on Ti6Al4V, *Tribol. Int.* 109 (2017) 285–296.
- [46] A.M.A. El-Rahman, R.H. Wei, Effect of ion bombardment on structural, mechanical, erosion and corrosion properties of Ti–Si–C–N nanocomposite coatings, *Surf. Coat. Technol.* 258 (2014) 320–328.
- [47] M.P. Dong, Y.B. Zhu, C.T. Wang, L. Shan, J.L. Li, Structure and tribocorrosion properties of duplex treatment coatings of TiSiCN/nitride on Ti6Al4V alloy, *Ceram. Int.* 45 (9) (2019) 12461–12468.